

Adaptive Reduced-Order Modeling for Non-Linear Fluid-Structure Interaction

Ali Thari^a, Vito Pasquariello^b, Niels Aage^c, Stefan Hickel^{a,*}

^a*Faculty of Aerospace Engineering, Technische Universiteit Delft, Kluyverweg 1, 2629 HS Delft, The Netherlands*

^b*Institute of Aerodynamics and Fluid Mechanics, Technische Universität München, Boltzmannstr. 15, 85748 Garching, Germany*

^c*Department of Mechanical Engineering, Technical University of Denmark, DK-2800 Lyngby, Denmark*

Abstract

We present an adaptive reduced-order model for the efficient time-resolved simulation of fluid-structure interaction problems with complex and non-linear deformations. The model is based on repeated linearizations of the structural balance equations. Upon each linearization step, the number of unknowns is strongly decreased by using modal reduction, which leads to a substantial gain in computational efficiency. Through adaptive re-calibration and truncation augmentation whenever a non-dimensional deformation threshold value is exceeded, we ensure that the reduced modal basis maintains arbitrary accuracy for small and large deformations. Our novel model is embedded into a partitioned, loosely coupled finite volume - finite element framework, in which the structural interface motion within the Eulerian fluid solver is accounted for by a conservative cut-element immersed-boundary method. Applications to the aeroelastic instability of a flat plate at supersonic speeds, to an elastic panel placed within a shock tube, and to the shock induced buckling of an inflated thin semi-sphere demonstrate the efficiency and accuracy of the method.

Keywords: fluid-structure interaction, reduced-order modeling, immersed boundary method, compressible flow

1. Introduction

Fluid-Structure Interaction (FSI) occurs in a very broad range of applications, such as blood flow through heart valves [30], flutter for aircraft wings [11] and shock-induced deformations of rocket nozzles and panels [15, 29]. FSI simulations involve two different branches of computational physics: Computational Fluid Dynamics (CFD), which is often based on an Eulerian finite-volume representation, and Computational Solid Mechanics (CSM), for which a finite-element discretization is frequently chosen.

FSI algorithms can be divided into monolithic and partitioned methods. The monolithic approach is characterized by solving the entire coupled system at once, i.e., solving a single set of discrete equations [21]. While this procedure may be time-consuming, it is robust, accurate and stable. On the other hand, the partitioned approach is frequently employed due to its computational efficiency and implementation conveniences, that is due to the possibility of using existing CSM and CFD solvers. Partitioned methods can further be classified as strongly or loosely coupled, where the distinction is based upon whether or not the complete set of coupling conditions at the conjoined FSI interface is satisfied. For the majority of compressible FSI applications, a loosely coupled method is sufficient [11]. When the densities of the fluid and the solid are comparable, loosely coupled methods may, however, suffer from the artificial added-mass effect, possibly leading to computational instabilities [6, 11]. Stability can be recovered by introducing sub-iterations [22], which however increase the computational cost significantly [14]. Badia et al. [1] have obtained very promising results by employing a Robin-type boundary condition at the FSI interface. Similarly, Banks et al. [4, 3] introduced so-called Added-Mass Partitioned algorithms to overcome the added-mass effect for incompressible flow as well as for light rigid bodies in compressible flow.

*Corresponding author.

Email address: S.Hickel@tudelft.nl (Stefan Hickel)

In practice, one of the main challenges is to keep the computational cost of time-resolved FSI simulations at a reasonable level without sacrificing the required accuracy. The time-stepping of FSI simulations is usually restricted by the resolution requirements of the fluid flow. Piperno et al. [31] proposed a sub-cycling approach, where the fluid solver is advanced multiple times before the structural solution is advanced in one large time step. The efficiency and stability of various sub-cycling methods are discussed by Farhat et al. [13]. As an alternative, the Reduced-Order Modeling (ROM) can be used to improve the efficiency of the CSM solver [36, 9, 17]. One of the first reported model reductions was presented by Rayleigh [35], who employed the Mode Superposition Method (MSM) to approximate the displacement field with a low number of free vibration modes. The method truncates the vibration modes of the structure at low number, i.e. $N \ll n$, where n is the number of degrees of freedom and N is the number of dynamically important modes. Several improvements for truncated modal superpositions have been proposed since then, one being the Static Correction Method (SCM) used by Besselink et al. [5], Wilson et al. [41] and Rixen [36], e.g.. This method accounts for the omitted modes by including the truncated modes statically, which leads to a more adequate representation of the modal loads. However, this method is only effective if the structure has very low natural frequencies. With the Modal Truncation Augmentation (MTA) method, Dickens et al. [7] introduced a dynamic correction of the load representation. MTA improves the overall accuracy compared to the SCM and is also effective for a broader frequency range [7]. Another popular reduction method is the Craig-Bampton Method (CBM) presented in [2] and the family of Component Mode Synthesis (CMS), see, e.g., Qu [33]. These methods divide the global FE structure into several substructures connected with an appropriate interface description. The CMS method is also known as Super Element Method in the sense that each substructure can be considered as a single finite element. Linear ROM approaches generally fail for non-linear problems. Mignolet et al. [25] reviewed ROMs for non-linear geometric structures based on indirect methodologies, where the non-linear stiffness terms are approximated by cubic polynomials. A key aspect of the ROM effort is to properly select the basis functions. The authors present a strategy that enriches the basis of free vibration modes by dual modes for capturing non-linear structural behavior. A set of non-linear static simulations with representative loads is needed to determine the dual modes, which are calculated based on the proper orthogonal decomposition of the series of non-linear displacement fields. Recently, [42] presented a ROM for flexible multi-body systems with large non-linear deflections, where the ROM is based on a combination of the CBM and cubic polynomials of the configuration dependent terms.

In this paper we derive an adaptive ROM (AROM) based on adaptive re-calibration of the reduced modal basis with MTA correction, which allows us to maintain arbitrary accuracy also in the case of large and non-linear structural deformations. The AROM is imbedded into the loosely coupled partitioned FSI algorithm proposed by Pasquariello et al. [28]. We employ a finite-volume method for solving the three-dimensional compressible Navier-Stokes equations on block-structured adaptive Cartesian grids and an unstructured finite-element method for the discretization of the structural domain. The time-varying interface between fluid and solid is accounted for by the cut-element based Immersed Boundary Method (IBM) that was introduced by Örley et al. [27] and then extended to deformable structures and compressible FSI applications by Pasquariello et al. [28]. The essential original contribution of this work is the development and demonstration of a novel FSI-AROM algorithm, capable of handling non-linear deformations accurately with high computational efficiency.

The paper is structured as follows: The governing equations of the fluid and structure and the numerical formulation are presented in Sections 2 and 3. The coupling algorithm for non-matching time-varying interfaces is presented in Section 4. The novel FSI-AROM method is derived in Section 5. In Section 6 we validate the FSI-AROM method for linear and non-linear problems, and demonstrate the prediction capabilities for flow-induced buckling of a three-dimensional thin semi-spherical shell. A final discussions and concluding remarks are given in Section 7.

2. Governing Equations

The domain of interest $\Omega = \Omega_F \cup \Omega_S$ is divided into non-overlapping fluid Ω_F and solid Ω_S subdomains with a conjoined interface $\Gamma = \Omega_F \cap \Omega_S$. The interface normal vector \mathbf{n}^Γ is assumed to point into the fluid domain. In the following a brief description of the mathematical models required for both subdomains is given. Unless specified otherwise, we use the Einstein summation convention.

2.1. Fluid

The fluid flow within the domain Ω_F is governed by the three-dimensional compressible Navier-Stokes equations

$$\frac{\partial \mathbf{w}}{\partial t} + \nabla \cdot \mathbf{H}(\mathbf{w}) = \mathbf{0}, \quad (1)$$

which describe the conservation of mass, linear momentum and total energy. We use Cartesian coordinates where $\nabla = \left(\frac{\partial}{\partial x_1}, \frac{\partial}{\partial x_2}, \frac{\partial}{\partial x_3} \right)$. The state vector \mathbf{w} and flux tensor $\mathbf{H}(\mathbf{w}) = [\mathbf{H}^{(1)}, \mathbf{H}^{(2)}, \mathbf{H}^{(3)}]$ are given as

$$\mathbf{w} = \begin{bmatrix} \rho_F \\ \rho_F u_1 \\ \rho_F u_2 \\ \rho_F u_3 \\ \rho_F e_t \end{bmatrix}, \quad \mathbf{H}^{(i)}(\mathbf{w}) = \begin{bmatrix} u_i \rho_F \\ u_i \rho_F u_1 + \delta_{i1} p - \tau_{i1} \\ u_i \rho_F u_2 + \delta_{i2} p - \tau_{i2} \\ u_i \rho_F u_3 + \delta_{i3} p - \tau_{i3} \\ u_i (\rho_F e_t + p) - u_k \tau_{ik} + q_i \end{bmatrix}, \quad (2)$$

where u_i is the velocity, ρ_F the fluid density, and $\rho_F e_t$ is the total energy density. The viscous stress tensor for a Newtonian fluid is

$$\tau_{ij} = \mu_F \left(\frac{\partial u_i}{\partial x_j} + \frac{\partial u_j}{\partial x_i} \right) + \lambda_F \frac{\partial u_k}{\partial x_k} \delta_{ij}, \quad (3)$$

where the first Lamé parameter is related to the dynamic viscosity μ_F according to Stoke's hypothesis: $\lambda_F = -2/3\mu_F$. The heat flux is evaluated according to Fourier's law,

$$q_i = -k \frac{\partial T}{\partial x_i}, \quad (4)$$

with the coefficient of thermal conductivity k . We consider air as a perfect gas with $\gamma = 1.4$ and specific gas constant of $R = 287.058 \frac{J}{kg \cdot K}$. The pressure p and temperature T are calculated from the definition of total energy

$$\rho_F e_t = \frac{1}{\gamma - 1} p + \frac{1}{2} \rho_F u_i u_i \quad (5)$$

and the ideal-gas equation of state

$$p = \rho_F R T. \quad (6)$$

2.2. Solid

The governing equations for the solid are based on the local form of the balance of linear momentum

$$\rho_{S;0} \frac{\partial^2 \mathbf{d}}{\partial t^2} = \nabla_0 \cdot \mathbf{P} + \hat{\mathbf{b}}_0, \quad (7)$$

which describes an equilibrium between the work done by the inertia, internal and external forces expressed in the underformed configuration. The vector of displacements is denoted by \mathbf{d} , $\rho_{S;0}$ is the material density of the solid, $\nabla_0 \cdot (\cdot)$ is the material divergence operator, $\mathbf{P} = \mathbf{F} \cdot \mathbf{S}$ is the first Piola-Kirchhoff stress tensor, where \mathbf{F} is the deformation gradient tensor, and external material body forces are represented by $\hat{\mathbf{b}}_0$. The second Piola-Kirchhoff stress tensor is

$$\mathbf{S} = \frac{\partial \Psi}{\partial \mathbf{E}}. \quad (8)$$

In this work, a hyperelastic Saint Venant-Kirchhoff material model is chosen. Its associated strain energy density function Ψ is given as

$$\Psi(\mathbf{E}) = \mu_S \mathbf{E} : \mathbf{E} + \frac{1}{2} \lambda_S (\mathbf{E} : \mathbf{I})^2, \quad (9)$$

where λ_S and μ_S are Lamé's first and second parameter. The Green-Lagrange strain tensor is defined as

$$\mathbf{E} = \frac{1}{2} (\mathbf{F}^T \cdot \mathbf{F} - \mathbf{I}) = \frac{1}{2} \left(\mathbf{D} + \mathbf{D}^T + \overbrace{\mathbf{D}^T \cdot \mathbf{D}}^{\text{non-linear}} \right), \quad (10)$$

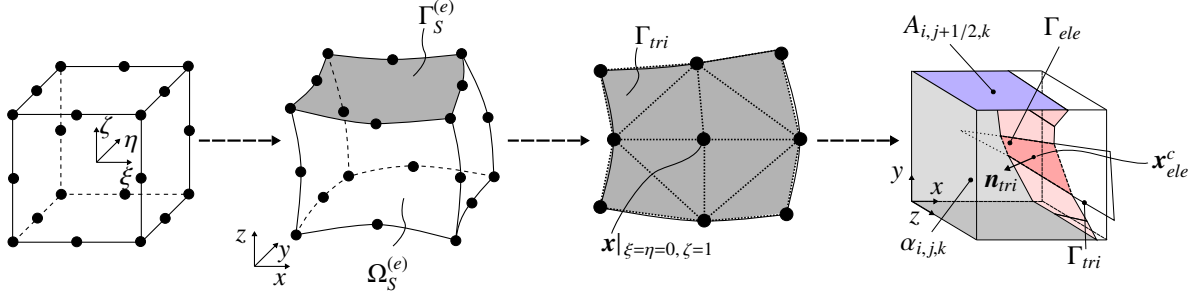


Figure 1: Schematic triangulation of a structural interface element $\Gamma_S^{(e)}$. Resulting interface triangles Γ_{tri} are used as an input for the cut-algorithm to compute individual cut-elements Γ_{ele} and cut-cell related geometric quantities.

and \mathbf{D} is the displacement gradient tensor. The Cauchy stress tensor $\boldsymbol{\sigma}_S$, also called true stress tensor, is defined as

$$\boldsymbol{\sigma}_S = \frac{1}{J} \mathbf{P} \cdot \mathbf{F}^T, \quad (11)$$

where J denotes the Jacobian determinant.

Boundary conditions need to be specified on $\partial\Omega_S = \Gamma_{S,D} \cup \Gamma_{S,N} \cup \Gamma$ to make Eq. (7) solvable. Two different types are considered in this work, namely Dirichlet $\Gamma_{S,D}$ and Neumann $\Gamma_{S,N}$ boundaries for which we either prescribe displacements $\hat{\mathbf{d}}$ or tractions $\hat{\mathbf{t}}$

$$\mathbf{d} = \hat{\mathbf{d}} \text{ on } \Gamma_{S,D} \text{ and } \mathbf{P} \cdot \mathbf{n}_0 = \hat{\mathbf{t}} \text{ on } \Gamma_{S,N}. \quad (12)$$

Here \mathbf{n}_0 denotes the unit normal vector in material configuration. Further, initial conditions for displacements and velocities must be specified:

$$\mathbf{d}^0 = \mathbf{d}(t=0) = \hat{\mathbf{d}}^0 \text{ on } \Omega_S \text{ and } \dot{\mathbf{d}}^0 = \dot{\mathbf{d}}(t=0) = \hat{\dot{\mathbf{d}}}^0 \text{ on } \Omega_S. \quad (13)$$

2.3. Fluid-structure interface conditions

The interface between the fluid and structure requires coupling conditions. Tractions on Γ have to be in equilibrium, that is,

$$\boldsymbol{\sigma}_S^\Gamma \cdot \mathbf{n}^\Gamma = \boldsymbol{\sigma}_F^\Gamma \cdot \mathbf{n}^\Gamma. \quad (14)$$

Herein, $\boldsymbol{\sigma}_S$ is the Cauchy stress tensor given by Eq. (11) and

$$\boldsymbol{\sigma}_F = -p\mathbf{I} + \boldsymbol{\tau} \quad (15)$$

denotes the fluid stress tensor comprising an inviscid and viscous contribution. In addition, the kinematic no-slip boundary condition

$$\frac{\partial \mathbf{d}^\Gamma}{\partial t} = \mathbf{u}^\Gamma \quad (16)$$

must be satisfied, which in case of an inviscid flow reduces to matching normal velocities on Γ

$$\frac{\partial \mathbf{d}^\Gamma}{\partial t} \cdot \mathbf{n}^\Gamma = \mathbf{u}^\Gamma \cdot \mathbf{n}^\Gamma. \quad (17)$$

3. Numerical models

3.1. Fluid

The compressible Navier-Stokes equations, Eq. (1), are discretized with a finite volume method based on the integral form

$$\int_{t^n}^{t^{n+1}} \int_{\Omega_{i,j,k} \cap \Omega_F} \frac{\partial \mathbf{w}}{\partial t} dV dt + \int_{t^n}^{t^{n+1}} \int_{\partial(\Omega_{i,j,k} \cap \Omega_F)} \mathbf{H}(\mathbf{w}) \cdot \mathbf{n} dS dt = 0, \quad (18)$$

where Gauss's theorem has been applied. The integral is taken over $\Omega_{i,j,k} \cap \Omega_F$, i.e., the part of a Cartesian computational cell $\Omega_{i,j,k}$ that belongs to the fluid domain Ω_F , and over the time step $\Delta t = t_{n+1} - t_n$. In order to account for the FSI interface within the fluid solver, which operates on Cartesian grids, we employ the cut-element IBM of Örley et al. [27] and Pasquariello et al. [28]. The discrete FSI interface is composed of several structural interface elements $\Gamma_S^{(e)}$. Each structural interface element $\Gamma_S^{(e)}$ is triangulated as shown exemplarily in Fig. 1 for a quadratic hexahedral element. The resulting interface triangles Γ_{tri} are used as an input for the IBM algorithm. A fluid cell that is cut by at least one interface triangle Γ_{tri} is referred to as a cut-cell. The fluid-solid interface within a cut-cell is composed of one or several cut-elements $\Gamma_{ele} = \Gamma_{tri} \cap \Omega_{i,j,k}$, each representing one or a part of one interface triangle, see Fig. 1. Applying a volume average of the conserved variables

$$\bar{\mathbf{w}}_{i,j,k} = \frac{1}{\alpha_{i,j,k} V_{i,j,k}} \int_{\Omega_{i,j,k} \cap \Omega_F} \mathbf{w} \, dx \, dy \, dz, \quad (19)$$

and considering (for demonstration purposes) a simple forward Euler time integration scheme leads to the following discrete form of Eq. (18)

$$\begin{aligned} \alpha_{i,j,k}^{n+1} \bar{\mathbf{w}}_{i,j,k}^{n+1} = & \alpha_{i,j,k}^n \bar{\mathbf{w}}_{i,j,k}^n + \frac{\Delta t}{\Delta x_i} \left[A_{i-1/2,j,k}^n \mathbf{H}_{i-1/2,j,k}^{(1)} - A_{i+1/2,j,k}^n \mathbf{H}_{i+1/2,j,k}^{(1)} \right] \\ & + \frac{\Delta t}{\Delta y_j} \left[A_{i,j-1/2,k}^n \mathbf{H}_{i,j-1/2,k}^{(2)} - A_{i,j+1/2,k}^n \mathbf{H}_{i,j+1/2,k}^{(2)} \right] \\ & + \frac{\Delta t}{\Delta z_k} \left[A_{i,j,k-1/2}^n \mathbf{H}_{i,j,k-1/2}^{(3)} - A_{i,j,k+1/2}^n \mathbf{H}_{i,j,k+1/2}^{(3)} \right] \\ & + \frac{\Delta t}{V_{i,j,k}} \chi_{i,j,k}. \end{aligned} \quad (20)$$

Herein $\alpha_{i,j,k}$ is the volume fraction of the cut-cell, $V_{i,j,k} = \Delta x_i \Delta y_j \Delta z_k$ is the total volume of cell $\Omega_{i,j,k}$ and A is the effective fluid wetted cell-face aperture, see also Fig. 1. The face averaged numerical fluxes across the regular cell faces are $\mathbf{H}^{(i)}$ and $\chi_{i,j,k} = \sum_{ele} \chi_{ele}$ denotes the integral flux across the interface $\Gamma_{i,j,k} = \sum_{ele} \Gamma_{ele}$, which is only present for a cut-cell. The interface fluxes χ_{ele} include the fluid stresses due to pressure and viscous effects, the resulting work at the interface, and heat transfer through the interface. For a detailed description of the cut-element IBM please refer to [27] and [28].

For the spatial reconstruction and numerical flux functions we either use the Adaptive Local Deconvolution Method (ALDM) by Hickel et al. [18, 19], or the 5th-order WENO (Weighted Essentially Non-Oscillatory) scheme by Liu et al. [24] with the HLLC flux [39]. In order to avoid modified interpolation stencils in the FV reconstruction near the interface, we assign special ghost fluid states that depend on the interface boundary conditions to non-cut fluid cells within the solid part of the domain [26, 28]. Finally, time integration is performed with a conditionally stable, explicit third-order Runge-Kutta scheme.

3.2. Solid

We cast the structural equations, Eq. (7), into their weak form by applying the principle of virtual work with virtual displacements $\delta \mathbf{d}$ and subsequently integrating the balance equation over the structural subdomain Ω_S . Following this procedure and applying Gauss's theorem yields

$$\int_{\Omega_S} \left(\rho_{S;0} \ddot{\mathbf{d}} \cdot \delta \mathbf{d} + \mathbf{S} : \delta \mathbf{E} - \hat{\mathbf{b}}_0 \cdot \delta \mathbf{d} \right) dV_0 - \int_{\Gamma_{S,N}} \hat{\mathbf{t}}_0 \cdot \delta \mathbf{d} dA_0 - \delta W_S^\Gamma = 0, \quad (21)$$

where dA_0 and dV_0 are infinitesimal surface and volume elements, respectively, and $\delta \mathbf{E}$ is a result of the variation of the strain expression in Eq. (10),

$$\delta \mathbf{E} = \frac{1}{2} \left(\mathbf{F}^T \delta \mathbf{D} + \delta \mathbf{D}^T \mathbf{F} \right). \quad (22)$$

The weak form, Eq. (21), represents the balance of virtual work δW , namely

$$\delta W_{inertia} + \delta W_{internal} - \delta W_{bodyforces} - \delta W_{traction} - \delta W_S^\Gamma = 0, \quad (23)$$

where the work at the FSI interface is δW_S^Γ . We use the FEM to discretize the integral equation (21) in space. The structural domain Ω_S is composed of n^e solid elements $\Omega_S^{(e)}$ with consistent basis functions for representing the displacement field. The semi-discrete form of Eq. (21) is then obtained by assembling the contributions of all elements $\Omega_S^{(e)}$, resulting in

$$\mathbf{M}\ddot{\mathbf{d}} + \mathbf{f}_{S;int}(\mathbf{d}) - \mathbf{f}_{S;ext}(\mathbf{d}) - \mathbf{f}_S^\Gamma = \mathbf{0}, \quad (24)$$

with the mass matrix \mathbf{M} ; the discrete acceleration vector $\ddot{\mathbf{d}}$ and the discrete displacement vector \mathbf{d} . The forces are divided into internal forces $\mathbf{f}_{S;int}$, external forces $\mathbf{f}_{S;ext}$ and interface forces \mathbf{f}_S^Γ resulting from the fluid.

In contrast to Pasquariello et al. [28], who used linear FE together with element technology based on Enhanced Assumed Strains to avoid locking phenomena, we use quadratic shape functions for interpolating the displacements on $\Omega_S^{(e)}$ unless stated otherwise. The final step is to discretize Eq. (24) in time. We employ the Hilber-Hughes-Taylor α -method [20] for the time integration. Due to its implicit character a coupled set of non-linear equations needs to be solved, which is done by the Newton-Raphson method.

4. Coupling methods

4.1. Load and motion transfer

The cut-cell IBM discretization inevitably leads to non-matching grids at the conjoined interface Γ and requires interpolation methods for the load transfer between both subdomains. Specifically, we search for the discrete force vector \mathbf{f}_S^Γ that results from the fluid tractions acting on the wetted structure. We follow the approach suggested by [12] and use the shape functions of $\Omega_S^{(e)}$ for interpolating the fluid loads on the adjacent structural nodes. Consider a single cut-element Γ_{ele} as shown in Fig. 1. The fluid forces \mathbf{f}_F^{ele} follow directly from the pressure and viscous contributions to the IBM interface flux $\chi = \sum_{ele} \chi_{ele}$ in Eq. (20). Since the structural interface, i.e., the triangulation Γ_{tri} , directly serves as an input for the IBM, there is no extra need for a pairing algorithm to associate a single face centroid \mathbf{x}_{ele}^c to the closest wet structural interface segment $\Gamma_S^{(e)}$. However, we have to determine the natural coordinates $\xi_{ele}^c(\mathbf{x}_{ele}^c)$ of this fluid point. This inverse mapping problem is solved iteratively with a Newton-Raphson method. Finally, the force contribution from a single cut-element to an individual node of the paired structural interface segment $\Gamma_S^{(e)}$ is given by

$$\mathbf{f}_{S,k}^\Gamma = N_k(\xi_{ele}^c) \mathbf{f}_F^{ele}, \quad (25)$$

where N_k denotes the shape function of the k -th structural node on $\Gamma_S^{(e)}$. Summing up the contributions of all cut-elements in Ω_F leads to the interface force vector \mathbf{f}_S^Γ . It is easy to verify that this interpolation guarantees a global conservation of loads over the interface by recalling that all shape functions at one specific location sum up to unity.

The cut-element IBM requires the velocity at the face centroid \mathbf{x}_{ele}^c for evaluating the work done at the interface, which contributes to the exchange term χ . We use the same interpolation strategy based on the shape functions of the structural domain

$$\mathbf{u}^{\Gamma;ele} = \sum_{k \in \Gamma_S^{(e)}} N_k(\xi_{ele}^c) \dot{\mathbf{d}}_k, \quad (26)$$

where $\dot{\mathbf{d}}_k$ is the velocity of the k -th structural node on $\Gamma_S^{(e)}$.

The motion of the structure within the fluid domain is accounted for by updating the cut-elements (and cut-cells) after each time step based on the triangulated interface Γ_{tri} [28]. Consequently the compatibility between the displacement fields of the structure and the fluid at the FSI interface is implicitly fulfilled in a discrete sense for all structural nodes $k \in \Gamma_S$ and no further interpolation is required.

4.2. Summary of the coupling procedure

We use an explicit, first-order in time accurate, loosely coupled FSI algorithm to advance the system from time level t^n to $t^{n+1} = t^n + \Delta t^n$. The main steps are summarized below:

1. At time level t^n the structural displacements $\mathbf{d}^{\Gamma;n}$ and velocities $\dot{\mathbf{d}}^{\Gamma;n}$ at the interface are used to update the cut-cell geometry. The triangulated interface Γ_{tri} , see Fig. 1, is used as an input for the cut-algorithm.
2. The fluid equations, Eq. (20), are advanced in time. The interface exchange term, as well as the ghost-cell methodology use known structural quantities at time level t^n . The interpolation of the structural interface velocities to the cut-elements is described in Section 4.1.
3. The newly computed fluid interface tractions $\boldsymbol{\sigma}_F^{\Gamma;n+1} \cdot \mathbf{n}^{\Gamma;n}$ are projected to the structural interface elements as described in Section 4.1 with the help of the shape functions of $\Omega_S^{(e)}$.
4. The structural system, Eq. (24), is solved and advanced in time with the projected fluid tractions from time level t^{n+1} imposed as additional Neumann boundary conditions.
5. Proceed to the next time step.

5. Adaptive Reduced-Order Model

5.1. Linearization and modal truncation

In this section, we propose a numerical framework for switching between a full FEM description and a more efficient Adaptive Reduced-Order Model (AROM) that maintains accuracy also when a structure undergoes large, i.e., non-linear, deformations. The algorithm is based on Taylor expansion around a reference state \mathbf{d}_{ref} . Linearizing Eq. (24) around this reference leads to

$$\mathbf{M}\ddot{\mathbf{d}}_{ref} + \mathbf{f}_{S;int}(\mathbf{d}_{ref}) - \mathbf{f}_{S;ext} - \mathbf{f}_S^\Gamma + \mathbf{M}(\ddot{\mathbf{d}} - \ddot{\mathbf{d}}_{ref}) + \frac{\partial \mathbf{f}_{S;int}(\mathbf{d}_{ref})}{\partial \mathbf{d}}(\mathbf{d} - \mathbf{d}_{ref}) = \mathbf{0}. \quad (27)$$

Notice that the reference state can be either a given initial condition or the FEM solution at the switching point between classical FEM and AROM. We introduce a new variable, $\delta \mathbf{d} = \mathbf{d} - \mathbf{d}_{ref}$, for the deflection with respect to the reference state \mathbf{d}_{ref} . Consequently, time derivatives of $\delta \mathbf{d}$ reduce to

$$\delta \dot{\mathbf{d}} = \dot{\mathbf{d}} \quad \text{and} \quad \delta \ddot{\mathbf{d}} = \ddot{\mathbf{d}}. \quad (28)$$

Rearranging Eq. (27) leads to

$$\mathbf{M}\delta \ddot{\mathbf{d}} + \mathbf{K}(\mathbf{d}_{ref})\delta \mathbf{d} = \mathbf{f}_{S;ext} + \mathbf{f}_S^\Gamma - \mathbf{f}_{S;int}(\mathbf{d}_{ref}), \quad (29)$$

where the tangent stiffness matrix $\mathbf{K}(\mathbf{d}_{ref})$ represents the Jacobian of the internal forces

$$\mathbf{K}(\mathbf{d}_{ref}) = \frac{\partial \mathbf{f}_{S;int}(\mathbf{d}_{ref})}{\partial \mathbf{d}}. \quad (30)$$

The initial conditions for $\delta \mathbf{d}$ are

$$\delta \mathbf{d}^0 = \mathbf{d}^n - \mathbf{d}_{ref} = \mathbf{0}, \quad (31)$$

$$\delta \dot{\mathbf{d}}^0 = \dot{\mathbf{d}}^n, \quad (32)$$

$$\delta \ddot{\mathbf{d}}^0 = \ddot{\mathbf{d}}^n, \quad (33)$$

where the superscript n denotes the (last) results obtained with the full FEM model, Eq. (24), before switching to AROM. Since this initial condition is also considered as the reference state, i.e., $\mathbf{d}^n = \mathbf{d}_{ref}$, the initial condition for the deflections $\delta \mathbf{d}^0$ is zero.

Equation (29) is expressed in the physical space; for reduced-order modeling we shrink the system of equations by the mode superposition method [35, 10]. In a first step, the eigenmodes of the structure are obtained by the following general eigenvalue problem of order m

$$\mathbf{K}(\mathbf{d}_{ref})\boldsymbol{\Phi} = \mathbf{M}\boldsymbol{\Phi}\boldsymbol{\Omega}^2, \quad (34)$$

where the columns of $\Phi = [\phi_1, \dots, \phi_m]$ are the orthonormalized (with respect to \mathbf{M}) eigenvectors (natural vibration modes) and $\Omega = \text{diag}(\omega_1, \dots, \omega_m)$ is a diagonal matrix listing associated eigenvalues (natural vibration frequencies). Note that Eq. (34) is only exact when the sizes of \mathbf{K} and Φ are equal. We define the following transformation from modal to physical space

$$\delta \mathbf{d} = \Phi \delta \mathbf{q}, \quad (35)$$

where $\delta \mathbf{q}$ denotes the vector of perturbations expressed in generalized coordinates, i.e. modal amplitudes. Substituting the latter expression into Eq. (29) and left-multiplying all terms with Φ^T leads to

$$\overbrace{(\Phi^T \mathbf{M} \Phi)}^{\mathbf{M}_G} \delta \ddot{\mathbf{q}} + \overbrace{(\Phi^T \mathbf{K} (\mathbf{d}_{\text{ref}}) \Phi)}^{\mathbf{K}_G(\mathbf{q}_{\text{ref}})} \delta \mathbf{q} = \overbrace{\Phi^T (\mathbf{f}_{S;\text{ext}} + \mathbf{f}_S^\Gamma)}^{\mathbf{p}_{\text{tot};G}} - \overbrace{\Phi^T (\mathbf{f}_{S;\text{int}}(\mathbf{d}_{\text{ref}}))}^{\mathbf{p}_{\text{int};G}(\mathbf{q}_{\text{ref}})}, \quad (36)$$

$$\mathbf{M}_G \delta \ddot{\mathbf{q}} + \mathbf{K}_G \delta \mathbf{q} = \mathbf{p}_{\text{tot};G} - \mathbf{p}_{\text{int};G}. \quad (37)$$

The size of the generalized matrices \mathbf{M}_G and \mathbf{K}_G directly depends on the number of eigenvectors considered, i.e., including the first N_{eig} eigenmodes reduces the system to rank N_{eig} . Furthermore, the principle of orthogonality implies that Eq. (36) can be written for the i -th mode as

$$\delta \ddot{q}_i + \omega_i^2 \delta q_i = \mathbf{p}_{i;\text{tot};G} - \mathbf{p}_{i;\text{int};G}, \quad (38)$$

recalling that \mathbf{M}_G is a unit matrix and \mathbf{K}_G is a diagonal matrix with eigenfrequencies squared on the diagonal [40]. An unconditionally stable Newmark scheme is used for time integration of the modal equations with the following initial conditions prescribed in modal space

$$\delta \mathbf{q}^0 = \mathbf{0}, \quad (39)$$

$$\delta \dot{\mathbf{q}}^0 = \Phi^T \mathbf{M} \dot{\mathbf{d}}_n, \quad (40)$$

$$\delta \ddot{\mathbf{q}}^0 = \Phi^T \mathbf{M} \ddot{\mathbf{d}}_n. \quad (41)$$

Equations (40) and (41) are derived using the orthogonality principle, i.e. $\Phi^T \mathbf{M} \Phi = \mathbf{I}$, and the relation in Eq. (35).

5.2. Modal truncation augmentation

The Modal Truncation Augmentation (MTA) method was derived by [7] in order to improve the representation of the load vector in modal space. The generalized loads can be computed as

$$\mathbf{p}_G = \Phi^T \mathbf{f}_{S;\text{tot}} - \Phi^T \mathbf{f}_{S;\text{int}}, \quad (42)$$

where $\mathbf{f}_{S;\text{tot}} = \mathbf{f}_{S;\text{ext}} + \mathbf{f}_S^\Gamma$ is the total load vector including external and interface loads. We transform the generalized forces back to the physical domain by

$$\tilde{\mathbf{f}}_S = \mathbf{M} \Phi \mathbf{p}_G, \quad (43)$$

which consequently results in a projection error that can be summarized in a residual

$$\mathbf{r} = (\mathbf{f}_{S;\text{tot}} - \mathbf{f}_{S;\text{int}}) - \tilde{\mathbf{f}}_S. \quad (44)$$

The MTA method attempts to correct for the projection error by appending a pseudo eigenvector $\tilde{\phi}$ to the original modal basis Φ . Note that the pseudo eigenvector does not satisfy the eigenvalue problem defined in Eq. (34) but it satisfies the orthogonality principle [7]. In a first step we solve for the displacements \mathbf{d}_{cor} due to the residual force vector

$$\mathbf{K}(\mathbf{d}_{\text{ref}}) \mathbf{d}_{\text{cor}} = \mathbf{r}. \quad (45)$$

Following this, we compute

$$\mathbf{K}_{\text{cor}} = \mathbf{d}_{\text{cor}}^{\text{T}} \mathbf{K}(\mathbf{d}_{\text{ref}}) \mathbf{d}_{\text{cor}}, \quad (46)$$

$$\mathbf{M}_{\text{cor}} = \mathbf{d}_{\text{cor}}^{\text{T}} \mathbf{M} \mathbf{d}_{\text{cor}}, \quad (47)$$

where \mathbf{K}_{cor} and \mathbf{M}_{cor} are the stiffness and mass matrices projected with respect to the displacement vector \mathbf{d}_{cor} . Note that in the special case of a single right-hand-side vector the matrices, \mathbf{K}_{cor} and \mathbf{M}_{cor} reduce to simple scalars and the following trivial eigenvalue problem can be formulated

$$K_{\text{cor}} \phi_{\text{cor}} = M_{\text{cor}} \phi_{\text{cor}} \omega_{\text{cor}}^2, \quad (48)$$

where ϕ_{cor} can be arbitrarily scaled. Following the work by [7], the pseudo eigenvector is calculated through $\tilde{\boldsymbol{\phi}} = \phi_{\text{cor}} \mathbf{d}_{\text{cor}}$, which in our case reduces to $\tilde{\boldsymbol{\phi}} = \mathbf{d}_{\text{cor}}$. The final step is to append the pseudo eigenvector to the original eigenvector matrix $\boldsymbol{\Phi}$ as follows

$$\boldsymbol{\Phi} \rightarrow \tilde{\boldsymbol{\Phi}} = [\boldsymbol{\Phi}, \mathbf{d}_{\text{cor}}], \quad (49)$$

and subsequently solve for the balance equation in modal space defined in Eq. (36).

5.3. Model re-calibration

Linear ROM generally fail for problems that involve large deformations because the structural properties (stiffness matrix and internal forces) used for constructing the ROM are valid only for small $\delta \mathbf{d}$. We solve this problem by updating the FEM discretization once the solution deviates significantly from the expansion point \mathbf{d}_{ref} used for linearization. This implies that also new augmented eigenmodes needs to be computed. Constructing and updating the ROM is expensive (due to the eigenvalue problem which needs to be solved) while applying it is very cheap. Efficiency for the proposed FSI method is achieved by re-using the reduced-order model as long as possible. We define a non-dimensional parameter

$$\epsilon = \frac{|\delta d_{\text{max}}|}{L}, \quad (50)$$

based on the maximum absolute deflection δd_{max} with respect to the reference frame \mathbf{d}_{ref} , i.e. the most recent linearization state, normalized by a characteristic length L of the structure. The ROM is adapted whenever ϵ exceeds a given threshold value. The efficiency and accuracy of the resulting *Adaptive* ROM (AROM) method depends on this threshold value. Note that the limit case $\epsilon = \infty$ corresponds to using the same ROM throughout the simulation, which minimizes the computational cost but will give inaccurate results if non-linear effects are large, while $\epsilon = 0$ corresponds to updating the ROM at each time step, which essentially yields the same accuracy as non-linear FEM at slightly increased computational cost.

6. Validation of the FSI-AROM algorithm

We validate and analyze the FSI-AROM algorithm for three application examples. The first problem considers a purely linear structure and hence the update threshold is set to $\epsilon = \infty$. We also refer to this case as the FSI-ROM approach, which implies that the ROM model is built only once at the beginning of the simulation. The second and third example include large deformations. We apply the FSI-AROM approach for these test cases and search for a suitable problem independent ϵ threshold value.

6.1. Supersonic panel flutter

The first example is the aeroelastic instability of a thin plate exposed to a supersonic inviscid flow. This FSI test problem is often considered in literature [38, 37, 28]. Dowell [8] has derived the critical flutter speed using linear stability theory and found that limit cycle oscillations occur at the critical Mach number of $\text{Ma}_{\infty;\text{crit}} = 2.0$. The computational setup together with its main parameters is sketched in Fig. 2a. The panel of length $l = 0.5$ m and thickness $t = 0.00135$ m is fixed at both ends and symmetry-type boundary conditions are applied at the front and back sides in the spanwise direction. We discretize the panel with 196 quadratic hexahedral elements in the streamwise direction and two elements along its thickness. Since we are dealing with a two-dimensional problem,

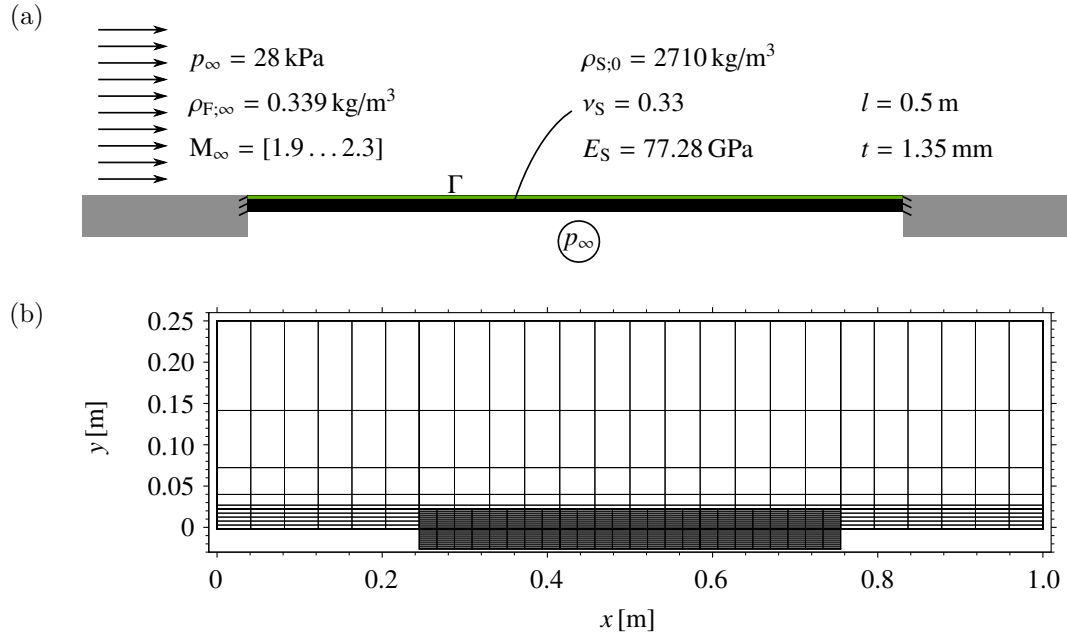


Figure 2: (a) Sketch of the flutter problem and main parameters. (b) FV grid used for the flutter analysis. Every 5th grid line is shown in the x and y direction. Figures adapted from [28].

we use one element across the span. The plate has a Young's modulus of $E_S = 77.28$ GPa, a Poisson's ratio of $\nu_S = 0.33$ and a density of $\rho_{S,0} = 2710$ kg/m³. The pressure of the free-stream is set to $p_\infty = 28$ kPa and the fluid density is $\rho_{F,\infty} = 0.339$ kg/m³. For the fluid domain a grid-converged resolution with a total number of 16,500 cells is used [28]. The grid is uniform with a cell size of $\Delta x = 4.25 \times 10^{-3}$ m and $\Delta y = 4.8 \times 10^{-4}$ m in proximity to the panel, see Fig. 2b. A cavity with a height of $h = 2.2 \times 10^{-2}$ m is defined below the panel to account for its motion within the IBM framework. Slip-wall boundary conditions apply except for the inflow and outflow patch. As the flow is supersonic, we prescribe all flow variables at the inflow and use linear extrapolation at the outflow boundary. We use ALDM for the flux discretization and a CFL number of 0.6 for the Runge-Kutta time-integration method. The upper panel surface is coupled to the fluid while a constant pressure of p_∞ is applied at the bottom side within the cavity. The cavity pressure is reduced by 0.1% the first 4 ms to provide an initial perturbation.

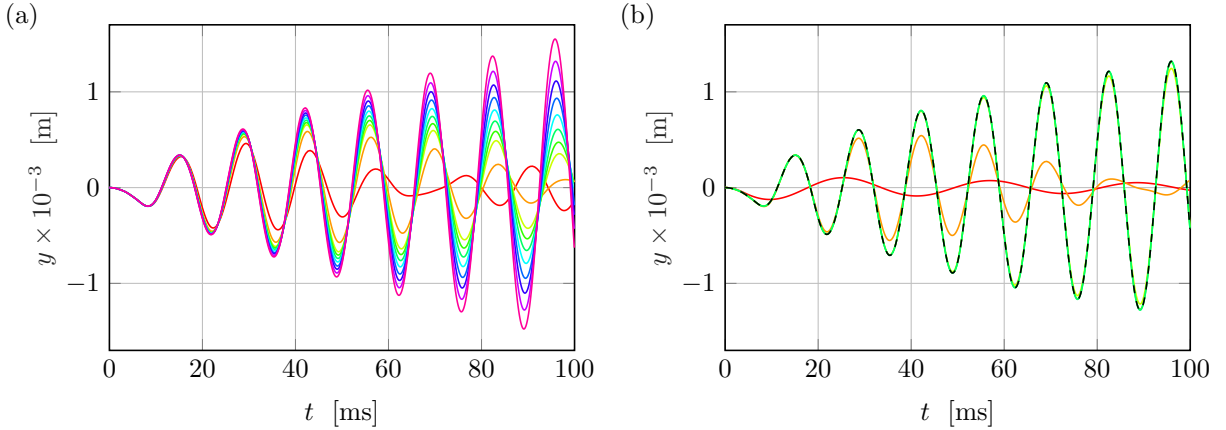


Figure 3: Panel flutter amplitudes recorded at $x = 0.6$ m. (a) Vertical displacement for various Mach numbers predicted by the FSI-ROM approach using 10 eigenmodes: (—) $Ma_\infty = 1.90$, (—) $Ma_\infty = 2.00$, (—) $Ma_\infty = 2.03$, (—) $Ma_\infty = 2.04$, (—) $Ma_\infty = 2.05$, (—) $Ma_\infty = 2.06$, (—) $Ma_\infty = 2.07$, (—) $Ma_\infty = 2.08$, (—) $Ma_\infty = 2.09$, (—) $Ma_\infty = 2.10$. (b) Sensitivity study with respect to the number of eigenmodes at $Ma_\infty = 2.09$: (—) $N_{eig} = 1$, (—) $N_{eig} = 3$, (—) $N_{eig} = 5$, (—) $N_{eig} = 7$, (—) $N_{eig} = 10$, (---) Linear FEM.

Main results for the flutter analysis are presented in Fig. 3 in terms of panel deflections evaluated at the streamwise position $x = 0.6$ m. In Fig. 3a, we show results obtained by the FSI-ROM approach including the first 10 structural eigenmodes for a Mach number range of $1.9 \leq Ma_\infty \leq 2.1$. Flutter onset is predicted to occur at a critical Mach number of $Ma_{\infty,crit} = 2.08$, with an error of 4.0% with respect to linear stability theory [8]. Almost identical results can be found in the work of Pasquariello et al. [28] who found a critical speed of $Ma_{\infty,crit} = 2.09$, and in the work of Sanches and Coda [37] who predicted flutter onset at $Ma_{\infty,crit} = 2.05$. Figure 3b shows the influence of the number of eigenmodes, N_{eig} , used in the modal database on the flutter prediction at $Ma_\infty = 2.09$. We observe monotonic convergence; 7 to 10 eigenmodes lead to an identical structural response as the reference FSI-FEM solution.

The reduced-order model significantly improves computational performance of the FSI simulation. The cost of the structural solver relative to the total simulation time amounts to $T_{S,ROM} = 2.42\%$ when using ROM, while solving the structural problem with the classical FEM approach costs $T_{S,FEM} = 77\%$ of the simulation time.

6.2. Elastic panel in a shock tube

Next, we study the impact of a shock wave on an elastic panel. This case is based on an experiment of Giordano et al. [16], and was later numerically investigated by Sanches and Coda [37] and Pasquariello et al. [28]. The setup is shown in Fig. 4. A right-moving $Ma = 1.21$ shock wave hits the rigid base plate and the elastic panel. The shock then propagates through the opening between the tip of the panel and the upper shock-tube wall and afterwards reflects back and forth between the end of the shock tube and the backside of the panel. We consider two cases, a panel with the length $l = 0.04$ m and one with $l = 0.05$ m. In both cases, the panel has a thickness of $b = 0.001$ m. The lower end of the panel is fixed at the rigid base plate and symmetry-type boundary conditions apply in spanwise

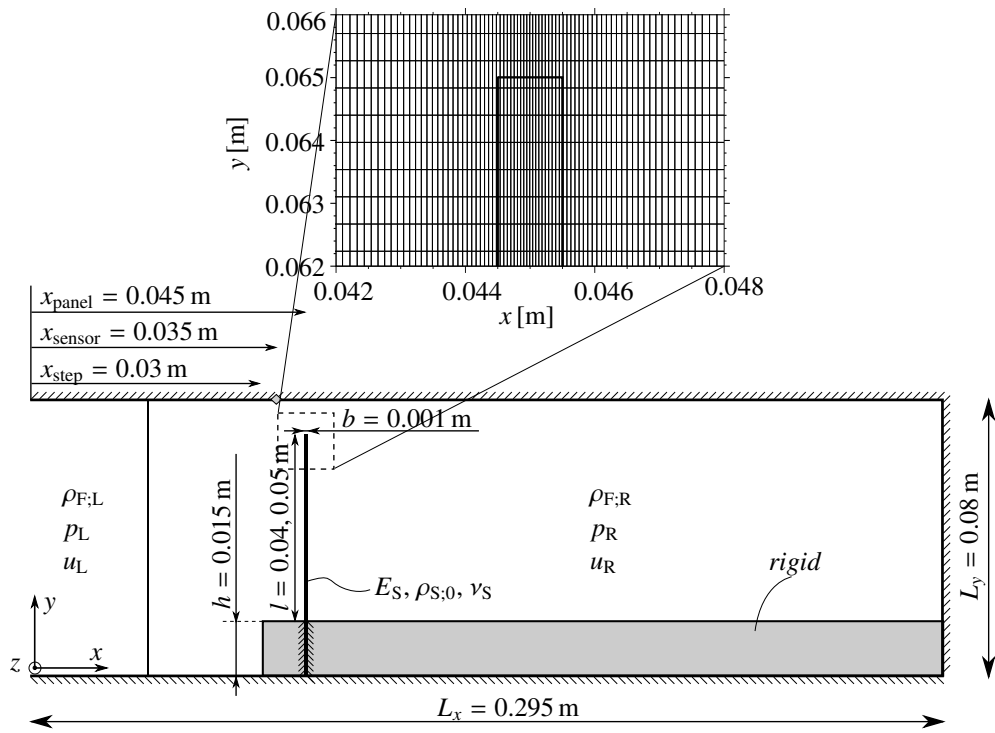


Figure 4: Main parameters for elastic panel in a shock tube adapted from Pasquariello et al. [28]. The FV mesh near the panel tip is schematically shown.

direction. The air is initially (pre-shock state) at rest and has a density of $\rho_{F;R} = 1.189 \text{ kg/m}^3$ and a static pressure of $p_R = 100 \text{ kPa}$. The post-shock conditions are $\rho_{F;L} = 1.616 \text{ kg/m}^3$, $p_L = 154 \text{ kPa}$ and $u_L = 109.68 \text{ m/s}$. The panel is made of steel and has a Young's modulus of $E_S = 220 \text{ GPa}$, a density of $\rho_S = 7600 \text{ kg/m}^3$ and a Poisson's ratio of $\nu_S = 0.33$. It is discretized using 55×2 quadratic hexahedral elements. The air flow is considered inviscid and compressible. We use ALDM for the flux discretization and a CFL number of 0.6 for time integration. The fluid domain is discretized with 123,400 cells with grid refinement around the panel, see Fig. 4. The inflow condition is based on Riemann invariants [32], and the remaining boundary patches mimic a slip-wall condition. The motion of the panel is mostly affected by its 1st bending mode, but in the following analyses we enrich the reduced model with the first 10 eigenmodes to ensure convergence.

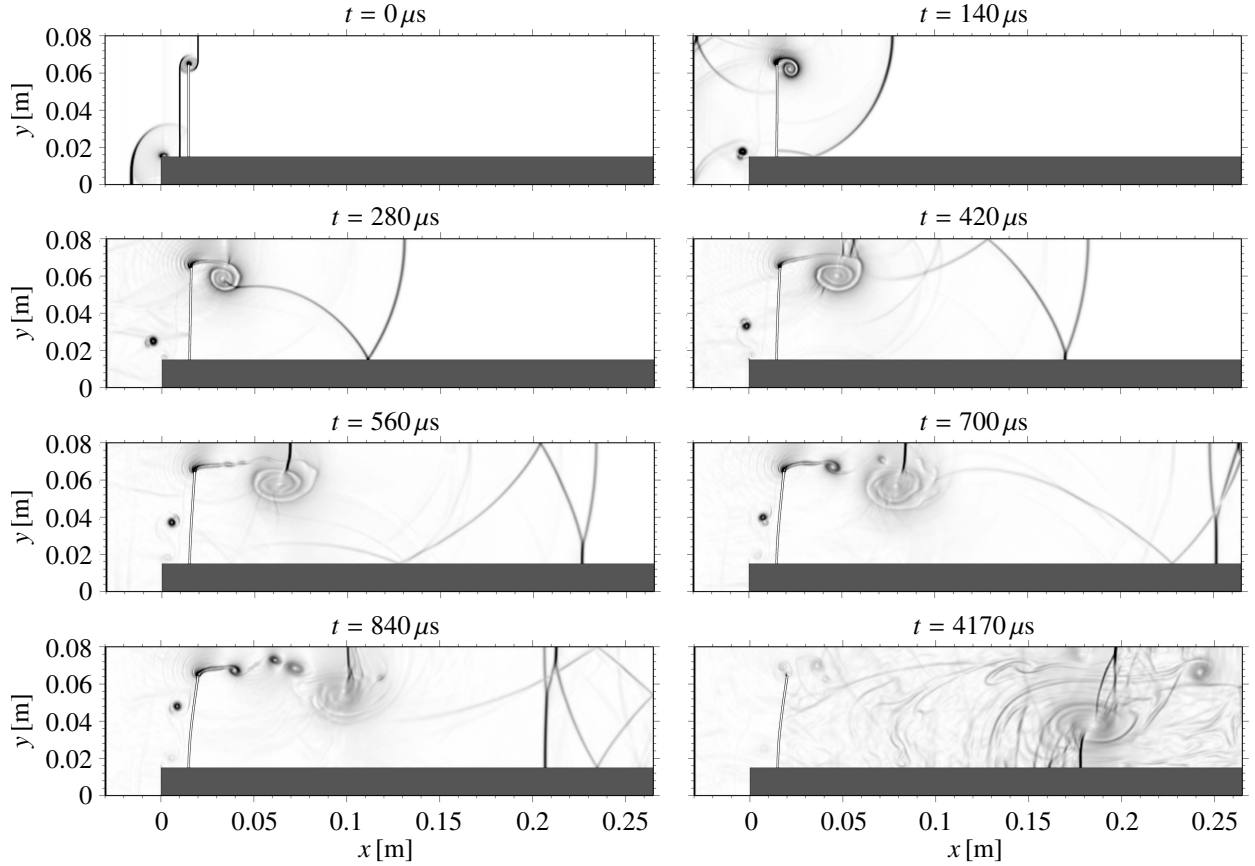


Figure 5: Density gradient magnitude $|\nabla\rho|$ for the $l = 0.05 \text{ m}$ panel at various time instances .

We start our analysis with results obtained by the non-linear FEM approach. In Fig. 5 we show contours of the density gradient magnitude $|\nabla\rho|$ at different times. Note that at $t = 0 \mu\text{s}$ the shock wave has already hit the panel, which is the same definition as used by [16]. At $t = 140 \mu\text{s}$ the shock has passed through the small gap between the tip and the upper wall. A reflected shock due to the collision with the panel is also seen. Subsequently, the vortex generated at the panel's tip grows and moves downstream, followed by a shedding of small-scale vortices after $t = 560 \mu\text{s}$. The initial shock wave is reflected at the shock tube's end and then interacts with the main vortex, which results in a complex flow field at $t > 840 \mu\text{s}$.

The panel-tip displacement history is plotted in Fig. 6a and Fig. 6b for the 0.04 m and 0.05 m panel length case, respectively. We compare our results to experimental data of Giordano et al. [16] and with numerical data from Sanches and Coda [37] and Pasquariello et al. [28]. All numerical simulations predict very similar oscillations of the panel. While all numerical data are in very good accordance with the experimental measurements for the shorter panel, the numerical results for the $l = 0.05 \text{ m}$ panel deviate from the experiments in amplitude and frequency, see

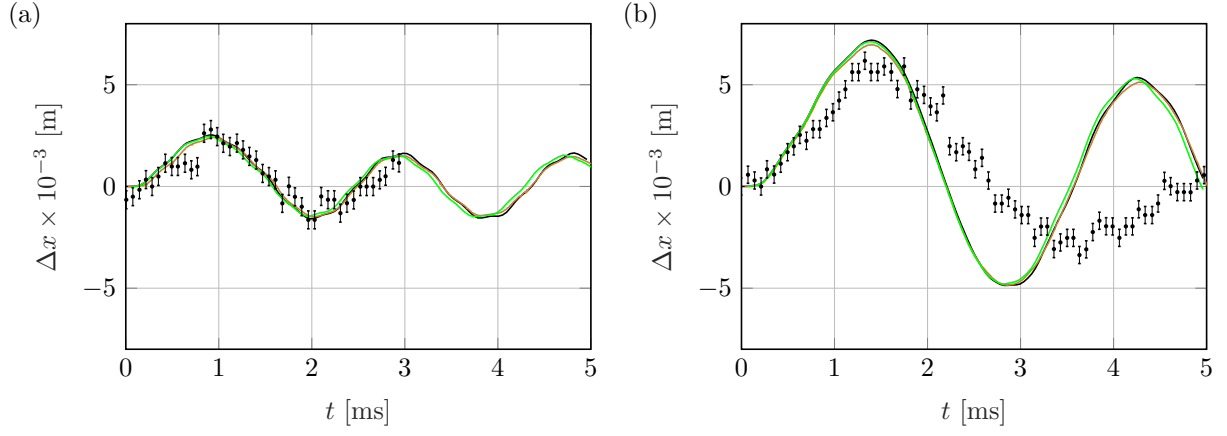


Figure 6: Time evolution of panel tip displacement for (a) $l = 0.04$ m and (b) $l = 0.05$ m: (—) present results, (—) [37], (—) [28]. Error bars denote experimental data from [16].

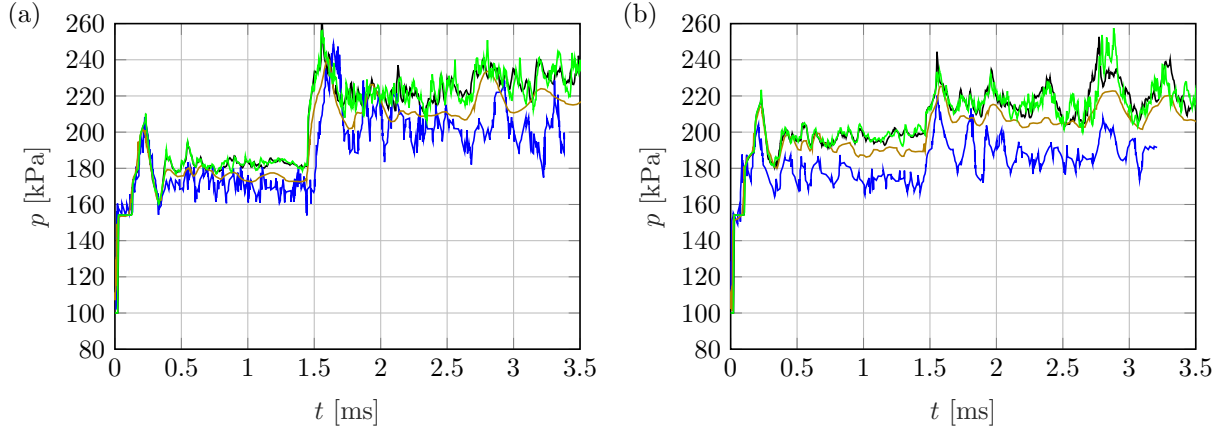


Figure 7: Pressure signal for the elastic panel of $l = 0.05$ m length recorded at x_{sensor} (see also Fig. 4): (—) present results; (—) numerical results of Sanches and Coda [37]; (—) numerical results of Pasquariello et al. [28]; (—) experimental results of Giordano et al. [16].

Fig. 6b). According to Giordano et al. [16], this might be due to a lack of damping in the structural model, although this should not affect the first oscillation period, or due to the stresses induced on the base, which are larger for the long panel and may provoke small deformations in this region and consequently influence the motion of the panel. The experiment conducted with the shorter panel implies lower stresses and thus smaller deformations of the base. Figure 7 shows the pressure signal recorded at x_{sensor} (see also Fig. 4) for both cases. Again, all results agree for the shorter panel, while larger systematic deviations between simulations and experiment can be observed for the $l = 0.05$ m panel. Note that a continuous drop of the experimental pressure is observed for $t > 2$ ms due to the reflected expansion waves within the shock tube. This phenomenon is not taken into account in the numerical simulations.

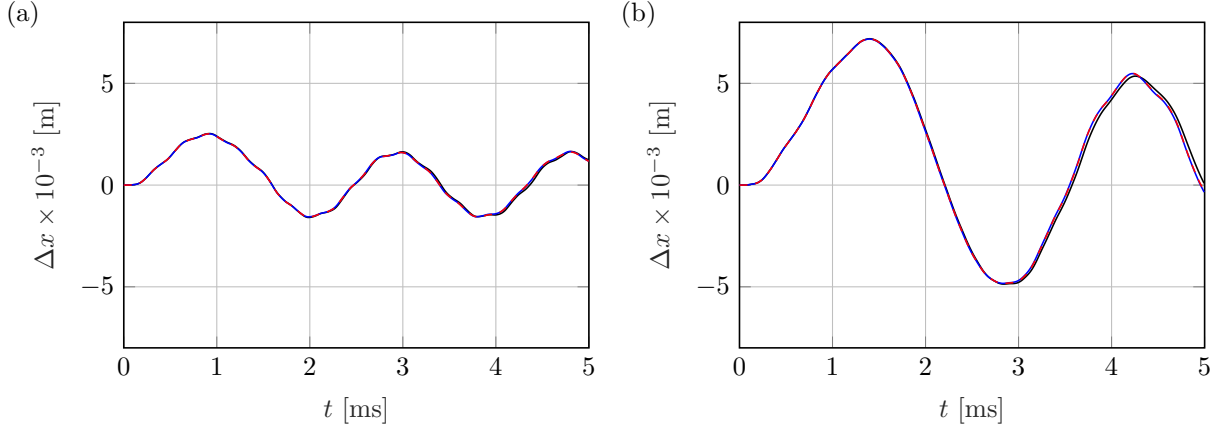


Figure 8: Time evolution of panel-tip displacement for (a) $l = 0.04$ m and (b) $l = 0.05$ m. (—) non-linear FEM; (—) linear FEM; (---) ROM with $N_{\text{eig}} = 10$.

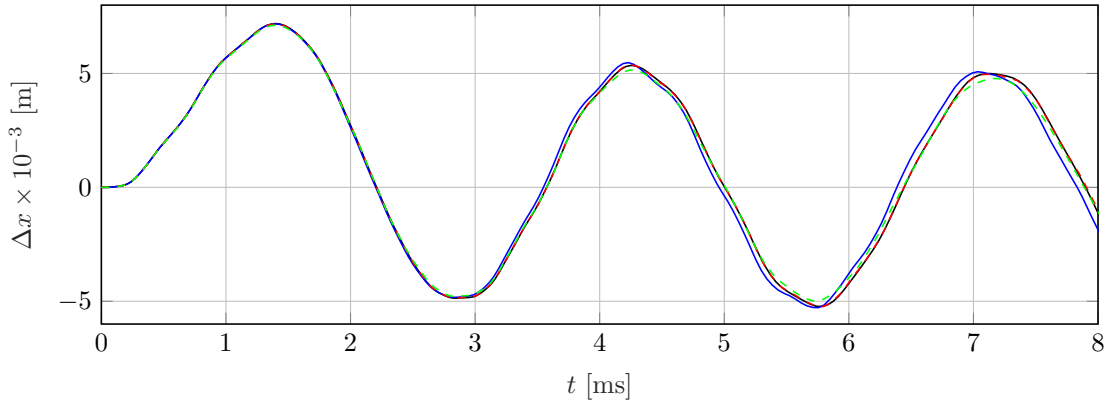


Figure 9: Long-time evolution of panel-tip displacement for $l = 0.05$ m: (—) non-linear FEM; (—) linear FEM; (---) AROM $\epsilon = 1.70 \times 10^{-3}$; (---) AROM $\epsilon = 4.30 \times 10^{-3}$ with $N_{\text{eig}} = 10$.

In the following we will evaluate the new reduced-order model. Figures 8a and 8b show the time evolution of the tip displacement for the short and long panel obtained with non-linear FEM, linear FEM and the ROM ($N_{\text{eig}} = 10$) approach. Deviations between linear FEM and linear ROM are negligible with a maximum error of approximately 0.01 %. With respect to the short panel, see Fig. 8a, all three structural models predict very similar displacements. Larger deviations between the non-linear and linear models can be observed for the long panel. We will therefore only consider the case with $l = 0.05$ m for the AROM simulations. Figure 9 shows the long-time evolution of the panel-tip displacement. Results obtained with the linear FEM show increased deviations from the non-linear FEM reference results with longer integration times. The AROM significantly improves the prediction accuracy. We

tested two threshold values ϵ for AROM (based on the reference length $L = l$). Results for $\epsilon = 1.70 \times 10^{-3}$ are almost identical to the non-linear FEM reference. A larger threshold value of $\epsilon = 4.30 \times 10^{-3}$ still gives significantly better results than the linear FEM approach at significantly lower computational cost.

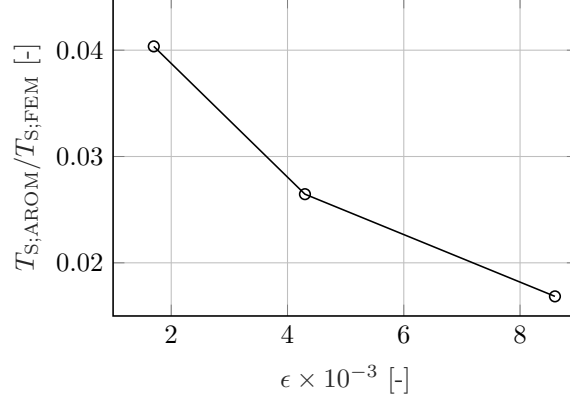


Figure 10: Efficiency for elastic panel in a shock tube: computational time of AROM normalized with the non-linear FEM simulation.

In Fig. 10, the computational cost of the adaptive ROM for different threshold values is compared with the cost of a non-linear FEM simulation. With the highest update frequency (lowest threshold value) the AROM requires less than 5 % of the CPU time of the non-linear FEM solver. As expected the performance gain can be even larger if the threshold is relaxed.

6.3. Buckling of a shock-loaded thin semi-spherical membrane

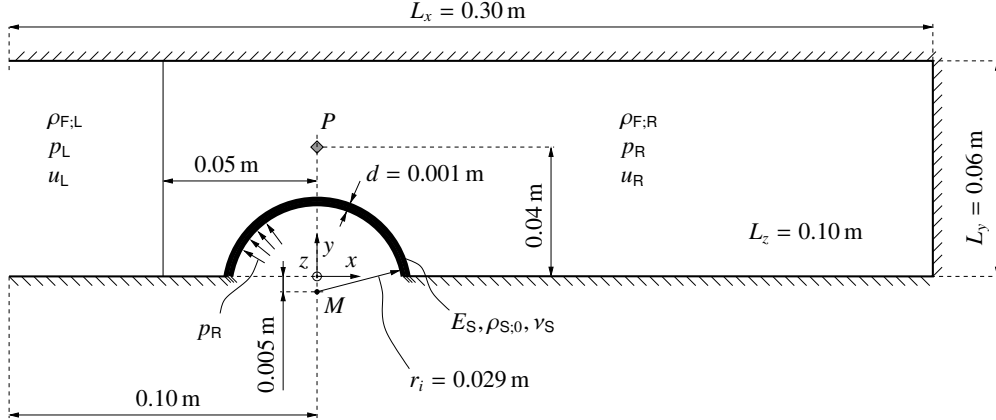


Figure 11: Buckling of a shock-loaded thin semi-spherical membrane: geometry, boundary conditions and initial conditions in the x - y plane, adapted from Pasquariello et al. [28].

The final application example is a three-dimensional FSI simulation of a thin shock-loaded membrane undergoing buckling [28]. It can be seen as an extension of the previous FSI cases to three-dimensional problems with complex structural behavior. Dynamic buckling is a non-linear structural phenomenon and highly sensitive with respect to any kind of imperfections, including grid resolution and modeling parameters [34]. This implies that tiny spatial variations in the loading of the structure may excite different buckling modes, which becomes even more evident for FSI problems, where the loads themselves are sensitive to the shape of the deformed body. Pasquariello et al. [28] found that the occurring buckling mode can be affected by the structural resolution, while the sensitivity with respect to the fluid grid plays a minor role for the present test case.

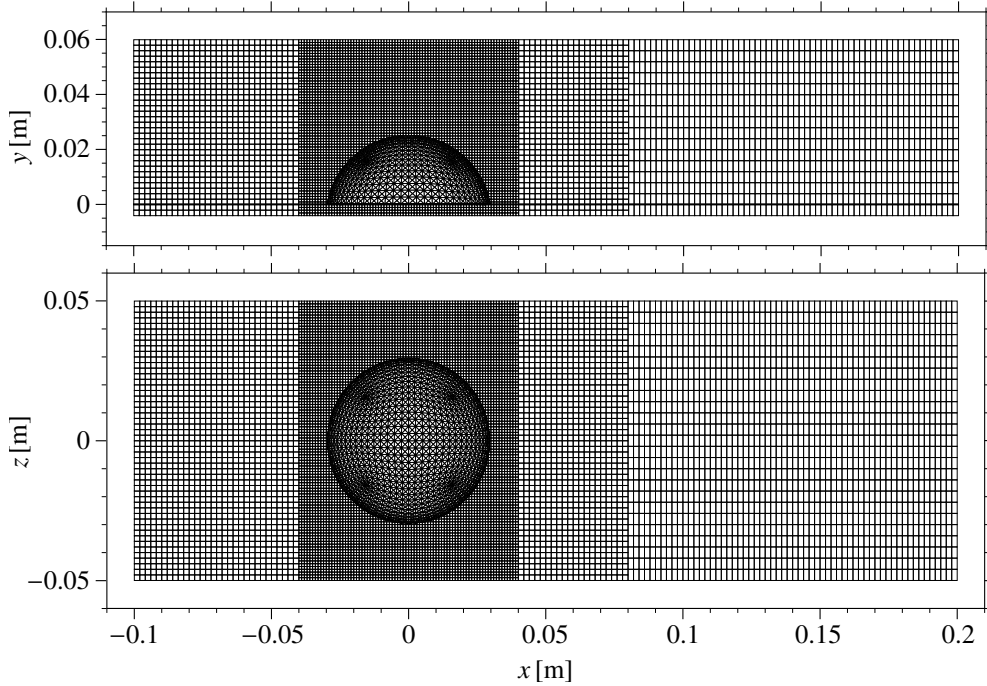


Figure 12: Fluid mesh and triangulated structural interface for buckling of a shock-loaded thin semi-spherical membrane.

The geometry and other setup details are shown in Fig. 11. The thin semi-spherical structure is hit by a right-running $Ma = 1.21$ shock wave, which is initialized at $x = -0.05$ m at $t = 0$ s. The shock propagates through the domain until it reflects back again at the end wall, which is located at $x = 0.2$ m. The initial pre-shock and post-shock conditions are the same as for the two-dimensional shock tube case, see Sec. 6.2. The membrane has a thickness of $d = 0.001$ m, an inner radius of $r_i = 0.029$ m, a Young's modulus of $E_S = 0.07$ GPa, a Poisson's ratio of $\nu_S = 0.35$ and a density of $\rho_{S,0} = 1000$ kg/m³. The reference length $L = 2r_i$ is used for the non-dimensional threshold ϵ . The membrane is discretized with 768 tri-linear hexahedral elements with two element layers in the thickness direction. Nodes belonging to the bottom of the semi-sphere have been fixed in all three directions. The inner volume of the sphere is pressurized at the nominal pre-shock value p_R in order to keep the membrane inflated in the absence of the shock.

The fluid domain is discretized with 616,000 FV cells. We use uniformly distributed cells with a size of 0.001 m in all three directions close to the coupling interface. The fluid solver uses a 5th-order WENO scheme with HLLC flux function and a CFL number of 0.6 for time integration. The FV mesh for the fluid solver and the triangulated structural interface Γ_S is shown in Fig. 12. With exception of the inflow patch, where we impose the post-shock state, slip-wall condition are used at all remaining boundaries.

Figure 13 depicts the pressure signal recorded at monitoring point P above the semi-sphere, see Fig. 11. The pressure signal has two distinct jumps, which indicate when the shock wave passes the sensor the first time ($t = 0.12$ ms) and the second time ($t = 1.22$ ms) after reflection at the end wall. The pressure signal is in excellent agreement with the data provided by Pasquariello et al. [28]. The sensor location is above the membrane and thus the pressure signal is not very sensitive to the motion of the structural interface. Contrary to the previous FSI examples, which were two-dimensional cases where a few number of eigenmodes sufficed, the current three-dimensional case is expected to require many more eigenmodes for capturing the local buckling of the structure. This is better understood by considering Fig. 14, where we show selected eigenmodes of the semi-sphere. Low-frequency modes represent a global motion of the structure and higher-frequency modes involve local deformations that are equally important for the present case.

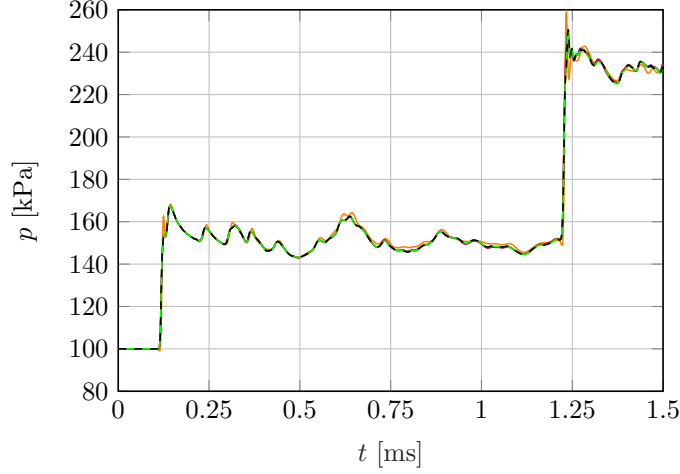


Figure 13: Pressure signal recorded above shock-loaded semi-spherical membrane at $(x, y, z) = (0, 0.04, 0)$ m: (---) non-linear FEM; (—) results of Pasquariello et al. [28]; (—) linear FEM; (—) linear ROM; (—) AROM $\epsilon = 1.70 \times 10^{-3}$.

In Fig. 15a, we compare linear and non-linear FEM results for the average root mean square (RMS) deflection to illustrate the necessity of employing non-linear structural analysis for the current FSI example. While the linear FSI-ROM (enriched with $N_{\text{eig}} = 100$ eigenmodes) perfectly matches the linear FEM results, we observe significant deviations from the non-linear FEM reference data. Such non-linear effects can be represented by our adaptive model: Figure 15b shows results obtained with our AROM with $\epsilon = 1.70 \times 10^{-3}$ and different numbers of eigenmodes $N_{\text{eig}} = \{12, 25, 50, 75, 100\}$. We observe clear convergence to the non-linear FEM reference with increasing number of eigenmodes. When certain buckling events during an unsteady simulation are not accurately resolved, the overall average deflection will ultimately differ. This becomes substantial when the system is enriched with an insufficient number of eigenmodes. $N_{\text{eig}} = 50$ eigenmodes reasonably cover the frequency space with global and local deflection modes and the displacement history predicted by AROM closely matches the non-linear FEM results. In addition, results obtained by Pasquariello et al. [28] are shown in Fig. 15a. We observe deviations from our non-linear FEM solution especially after the membrane collapses, i.e., after $t \geq 1.2$ ms, which is not unexpected as multi-mode buckling is highly sensitive to numerical details [34].

Next we study the effect of the threshold value ϵ for updating the AROM. In Fig. 16, the time-evolution of the RMS displacements are shown for various tolerances in the left column, and relative errors with respect to the non-linear FEM reference solution are shown in the right column. For the error plots we blank the initial part, where very small reference displacements values would lead to ambiguously high relative errors. The cases with $\epsilon = 17 \times 10^{-3}$ and $\epsilon = 12.9 \times 10^{-3}$ have maximum errors above 25% and 10%, respectively, with the largest errors with $N_{\text{eig}} = 50$ eigenmodes. For the highest update frequency for AROM, i.e., the smallest threshold value of $\epsilon = 1.70 \times 10^{-3}$, $N_{\text{eig}} = 50$ modes lead to a maximum error of 5.5% occurring at approximately $t = 1.5$ ms. Extending the modal base to $N_{\text{eig}} = 75$ and $N_{\text{eig}} = 100$ eigenmodes, while keeping the same threshold value, further reduces the maximum error down to 1.6% (at $t = 1.5$ ms) and 0.7% (at $t = 1.2$ ms), respectively. In general, a threshold of $\epsilon = 8.60 \times 10^{-3}$ results in acceptable errors of less than 5.0% when considering $N_{\text{eig}} = 75$ or $N_{\text{eig}} = 100$ eigenmodes.

Figure 17 shows a qualitative comparison between AROM and non-linear FEM results for the deformation at two time instances. The depicted AROM results were obtained with an update threshold of $\epsilon = 4.30 \times 10^{-3}$ and $N_{\text{eig}} = 75$ eigenmodes. The top row shows the deformation at $t = 1.2$ ms, just before the shock wave hits the structure for the second time. We clearly identify a compression of the windward side initiated by the initial shock passage. At $t = 1.5$ ms (bottom row), the shock has passed the sphere a second time and high-order (local) buckling becomes significant. We observe excellent agreement between the non-linear FEM and AROM results.

We compare the computational cost $T_{S;\text{AROM}}$ of the various AROM simulations normalized with the cost of the

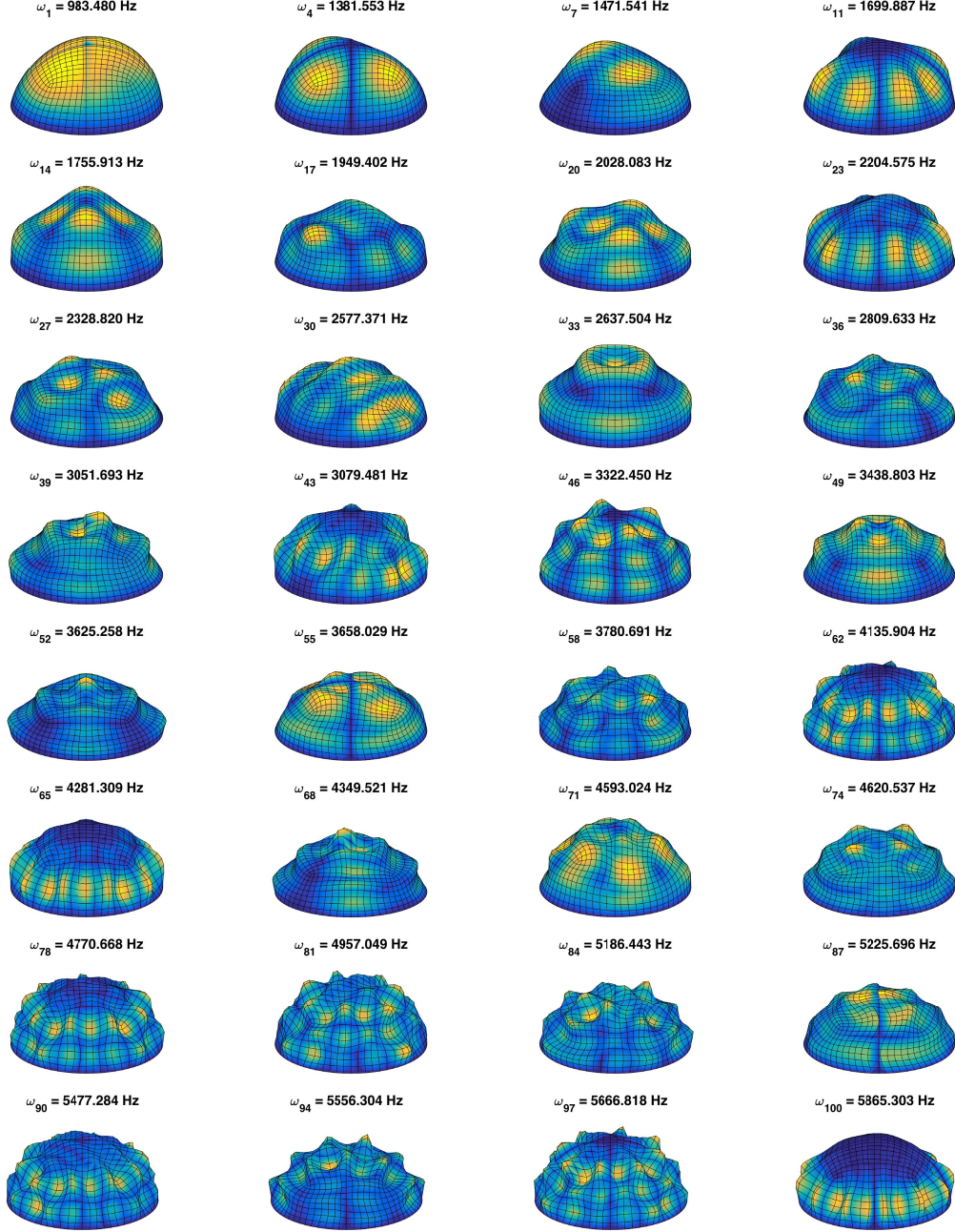


Figure 14: Selected eigenmodes of the semi-spherical membrane. The mode number and natural frequency is indicated above each sub-figure. The color scale ranges from dark-blue to bright-yellow and represents the magnitude of the deflection mode.

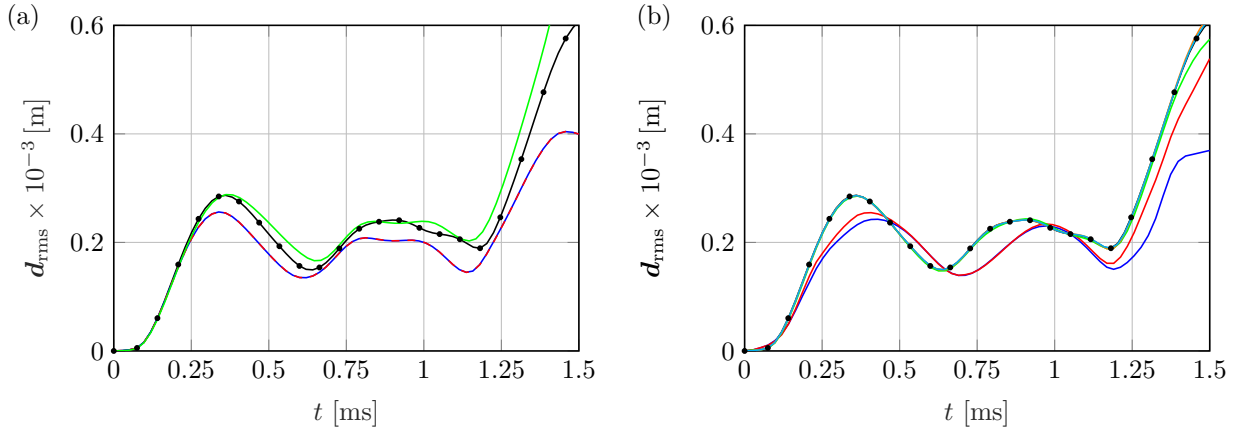


Figure 15: RMS node displacements for shock-induced buckling of thin semi-spherical membrane: (a) (\rightarrow) non-linear FEM; (\rightarrow) results of Pasquariello et al. [28]; (\rightarrow) linear FEM; (\rightarrow) ROM with $N_{\text{eig}} = 100$. (b) (\rightarrow) non-linear FEM; AROM with $\epsilon = 1.70 \times 10^{-3}$ and (\rightarrow) $N_{\text{eig}} = 12$, (\rightarrow) $N_{\text{eig}} = 25$, (\rightarrow) $N_{\text{eig}} = 50$, (\rightarrow) $N_{\text{eig}} = 75$, (\rightarrow) $N_{\text{eig}} = 100$.

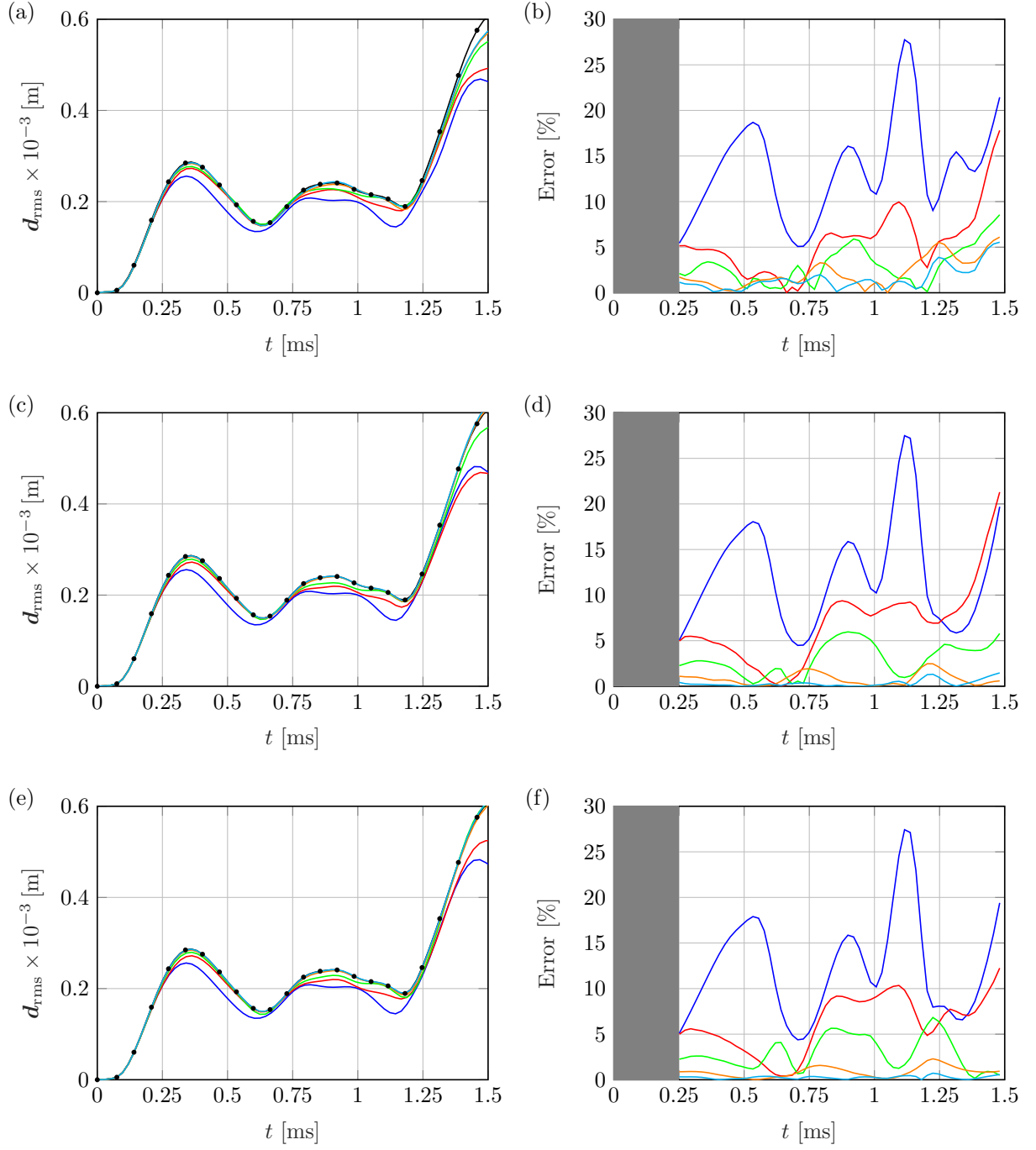


Figure 16: RMS node displacements for shock-induced buckling (left column) and associated relative errors (right column) with respect to the non-linear FEM solution for (a)-(b) $N_{\text{eig}} = 50$, (c)-(d) $N_{\text{eig}} = 75$, and (e)-(f) $N_{\text{eig}} = 100$: (—•—) non-linear FEM; (—) AROM $\epsilon = 17.0 \times 10^{-3}$; (—) AROM $\epsilon = 12.9 \times 10^{-3}$; (—) AROM $\epsilon = 8.60 \times 10^{-3}$; (—) AROM $\epsilon = 4.30 \times 10^{-3}$; (—) AROM $\epsilon = 1.70 \times 10^{-3}$.

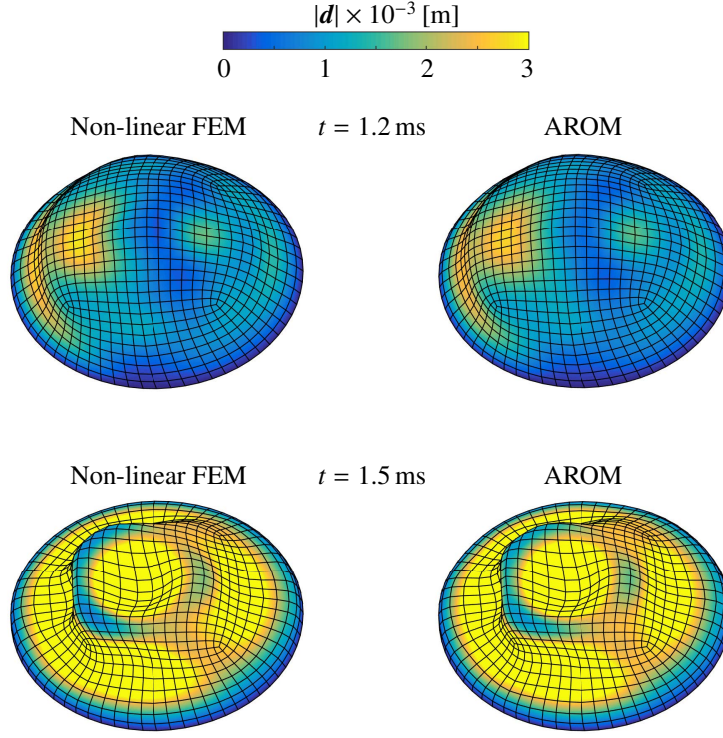


Figure 17: Deformation magnitude contours at two time-instances predicted by the full non-linear FEM (left column) and the AROM with $\epsilon = 4.30 \times 10^{-3}$ and $N_{\text{eig}} = 75$ (right column). A scale factor of 350 has been applied for all contours.

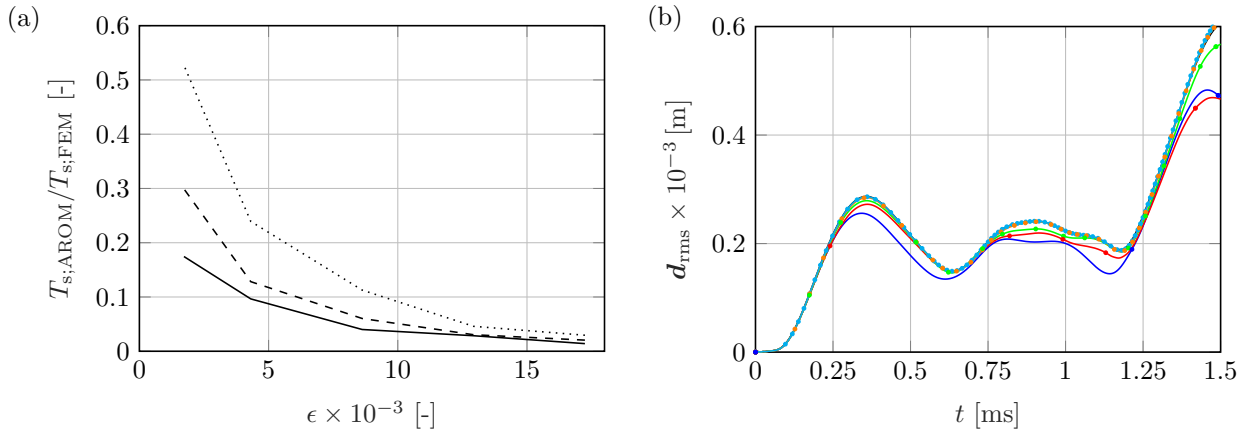


Figure 18: (a) Relative time-cost of the structural part as a function of ϵ . (—) AROM with $N_{\text{eig}} = 50$, (---) AROM with $N_{\text{eig}} = 75$, (·····) AROM with $N_{\text{eig}} = 100$. (b) RMS node displacements for AROM with $N_{\text{eig}} = 75$: (—) non-linear FEM, (—) AROM $\epsilon = 17.0 \times 10^{-3}$, (—) AROM $\epsilon = 12.9 \times 10^{-3}$, (—) AROM $\epsilon = 8.60 \times 10^{-3}$, (—) AROM $\epsilon = 4.30 \times 10^{-3}$, (—) AROM $\epsilon = 1.70 \times 10^{-3}$. Every mark represents the instance of a ROM update.

non-linear FEM case $T_{S,FEM}$ in Fig. 18a. The symbols in Fig. 18b exemplarily depicts the update instances of AROM for $N_{eig} = 75$ eigenmodes when using different threshold values. In general, the performance gain depends on the number of modes included in the ROM database and the update frequency of AROM, i.e., the threshold value ϵ . Choosing the lowest threshold ($\epsilon = 1.70 \times 10^{-3}$) considered in this example saves approximately 50 % (with $N_{eig} = 100$ eigenmodes), 70 % (with $N_{eig} = 75$ eigenmodes) and 80 % (with $N_{eig} = 50$ eigenmodes) with respect to non-linear FEM. The threshold-value and mode-number dependence of the computational cost stems mostly from the eigenvalue solver. We solve the eigenvalue problem using a shift-invert method, which is very efficient for finding the lowest eigenvalues, while it results in strongly increased computational cost when searching for relatively high eigenvalues [23].

7. Conclusions

We proposed a computationally efficient and accurate Reduced-Order Model (ROM) for non-linear aeroelasticity simulations that require a time-resolved representation of the fluid flow and structural dynamics. The model significantly reduces the computational cost of the structural-dynamics solver through augmented modal truncation of a non-linear finite-element model linearized around a loaded and deformed base state. Linear modal superposition alone would lead to large errors in the case of large deformations, because the structural properties used for constructing the ROM are valid only for small deflections from the reference configuration. We solved this problem by adaptive re-calibration and truncation augmentation, which are performed whenever non-linear effects affect the structural properties like the stiffness matrix and internal forces. The resulting Adaptive ROM (AROM) can maintain arbitrary accuracy, which is only limited by the baseline finite-element discretization, for small and large deformations.

The effectiveness of the AROM is controlled by a non-dimensional displacement-based parameter that determines when a re-calibration step is initiated. Constructing and updating the modal basis is expensive due to the eigenvalue problem that needs to be solved. Efficiency is achieved by re-using the modal basis as long as possible. With very small threshold values, the AROM is adapted very frequently and the computational results, but also the computational cost, converge to a space and time resolved non-linear finite-element simulation. A too large threshold, on the other hand, leads to an essentially linear model and possibly inaccurate results. We performed sensitivity studies for several test cases and found that a non-dimensional threshold value of about 4×10^{-3} leads to the best balance between computational efficiency and accuracy for all cases.

The proposed method can be used with any partitioned Fluid-Structure Interaction (FSI) solver framework; the algorithm is independent of the baseline discretizations of fluid and structure. Our loosely coupled FSI implementation employs an unstructured finite-element discretization of the structural domain and a finite-volume method for solving the three-dimensional compressible Navier-Stokes equations on block-structured grids with a cut-element immersed-boundary method for representing the time-varying interface between fluid and solid. Using this FSI solver framework, the accuracy and efficiency of the AROM have been demonstrated and quantified for two- and three-dimensional fluid-structure interaction problems: We have shown that the model is accurate and very efficient for predicting the onset of flutter in supersonic flows. The AROM approach can by construction yield predictions with any required accuracy for shock-loaded structures undergoing large deformations, for which classical, i.e., linear ROM fail. The AROM also correctly reproduced the multi-modal buckling of a thin semi-spherical membrane with the same accuracy as non-linear finite-element method and at significantly reduced computational cost.

References

- [1] Badia, S., Nobile, F., Vergara, C., 2008. Fluid structure partitioned procedures based on Robin transmission conditions. *Journal of Computational Physics* 227 (14), 7027–7051.
- [2] Bampton, M. C. C., Craig, JR., R. R., 1968. Coupling of substructures for dynamic analyses. *AIAA Journal* 6 (7), 1313–1319.
- [3] Banks, J., Henshaw, W., Schwendeman, D., 2014. An analysis of a new stable partitioned algorithm for FSI problems. Part I: incompressible flow and elastic solids. *Journal of Computational Physics* 269, 108–137.
- [4] Banks, J., Henshaw, W., Sjögreen, B., 2013. A stable FSI algorithm for light rigid bodies in compressible flow. *Journal of Computational Physics* 245, 399–430.
- [5] Besselink, B., Tabak, U., Lutowska, A., van de Wouw, N., Nijmeijer, H., Rixen, D., Hochstenbach, M., Schilders, W., 2013. A comparison of model reduction techniques from structural dynamics, numerical mathematics and systems and control. *Journal of Sound and Vibration* 332 (19), 4403–4422.

- [6] Causin, P., Gerbeau, J., Nobile, F., 2005. Added-mass effect in the design of partitioned algorithms for fluid-structure problems. *Computer Methods in Applied Mechanics and Engineering* 194 (42-44), 4506–4527.
- [7] Dickens, J. M., J. M., N., Wittbrodt, M. J., 1995. A critique of mode acceleration and modal truncation augmentation methods for modal response analysis. *Computers & Structures* 62 (6), 985–998.
- [8] Dowell, E. H., 1974. *Aeroelasticity of plates and shells*. Springer, Leyden.
- [9] Dowell, E. H., 1996. Eigenmode analysis in unsteady aerodynamics: Reduced-order models. *AIAA Journal* 34 (8), 1578–1583.
- [10] Dowell, E. H., Hall, K. C., 2001. Modeling of fluid-structure interaction. *Annual Review of Fluid Mechanics* 33, 445–490.
- [11] Farhat, C., Lesoinne, M., 2000. Two efficient staggered algorithms for the serial and parallel solution of three-dimensional nonlinear transient aeroelastic problems. *Computer Methods in Applied Mechanics and Engineering* 182 (3-4), 499–515.
- [12] Farhat, C., Lesoinne, M., Le Tallec, P., 1998. Load and motion transfer algorithms for fluid/structure interaction problems with non-matching discrete interfaces: Momentum and energy conservation, optimal discretization and application to aeroelasticity. *Computer Methods in Applied Mechanics and Engineering* 157 (1-2), 95–114.
- [13] Farhat, C., Lesoinne, M., Stern, P., Lantri, S., 1997. High performance solution of three-dimensional nonlinear aeroelastic problems via parallel partitioned algorithms: Methodology and preliminary results. *Advances in Engineering Software* 28 (1), 43–61.
- [14] Farhat, C., van der Zee, K. G., Geuzaine, P., 2006. Provably second-order time-accurate loosely-coupled solution algorithms for transient nonlinear computational aeroelasticity. *Computer Methods in Applied Mechanics and Engineering* 195 (17-18), 1973–2001.
- [15] Garelli, L., Paz, R. R., Storti, M. A., 2010. Fluid structure interaction study of the start-up of a rocket engine nozzle. *Computers & Fluids* 39 (7), 1208–1218.
- [16] Giordano, J., Jourdan, G., Burtischell, Y., Medale, M., Zeitoun, D. E., Houas, L., 2005. Shock wave impacts on deforming panel, an application of fluid-structure interaction. *Shock Waves* 14 (1), 103–110.
- [17] Hall, K., Thomas, J., Dowell, E., 1999. Reduced-order modelling of unsteady small-disturbance flows using a frequency-domain proper orthogonal decomposition technique. *AIAA paper*, No. 99–0655.
- [18] Hickel, S., Adams, N. A., Domaradzki, J. A., 2006. An adaptive local deconvolution method for implicit LES. *Journal of Computational Physics* 213 (1), 413–436.
- [19] Hickel, S., Egerer, C., Larsson, J., 2014. Subgrid-scale modeling for implicit large eddy simulation of compressible flows and shock-turbulence interaction. *Physics of Fluids* 26 (10), 106101.
- [20] Hilber, H. M., Hughes, T. J. R., Taylor, R. L., 1977. Improved numerical dissipation for time integration algorithms in structural dynamics. *Earthquake Engineering & Structural Dynamics* 5 (3), 283–292.
- [21] Klöppel, T., Popp, A., Küttler, U., Wall, W. A., 2011. Fluid - structure interaction for non-conforming interfaces based on a dual mortar formulation. *Computer Methods in Applied Mechanics and Engineering* 200 (45-46), 3111–3126.
- [22] Küttler, U., Wall, W. A., 2008. Fixed-point fluid-structure interaction solvers with dynamic relaxation. *Computational Mechanics* 43 (1), 61–72.
- [23] Lehoucq, R. B., Sorensen, D. C., Yang, C., 1997. *ARPACK Users' Guide: Solution of Large Scale Eigenvalue Problems with Implicitly Restarted Arnoldi Methods*.
- [24] Liu, X.-D., Osher, S., Chan, T., 1994. Weighted essentially non-oscillatory schemes. *Journal of Computational Physics* 115 (1), 200–212.
- [25] Mignolet, M. P., Przekop, A., Rizzi, S. A., Spottswood, S. M., 2013. A review of indirect/non-intrusive reduced order modeling of nonlinear geometric structures. *Journal of Sound and Vibration* 332 (10), 2437–2460.
- [26] Mittal, R., Dong, H., Bozkurttas, M., Najjar, F., Vargas, A., von Loebbecke, A., 2008. A versatile sharp interface immersed boundary method for incompressible flows with complex boundaries. *Journal of Computational Physics* 227 (10), 4825–4852.
- [27] Örley, F., Pasquariello, V., Hickel, S., Adams, N. A., 2015. Cut-element based immersed boundary method for moving geometries in compressible liquid flows with cavitation. *Journal of Computational Physics* 283, 1 – 22.
- [28] Pasquariello, V., Hammerl, G., Örley, F., Hickel, S., Danowski, C., Popp, A., Wall, W. A., Adams, N. A., 2016. A cut-cell finite volume – finite element coupling approach for fluid-structure interaction in compressible flow. *Journal of Computational Physics* 307, 670–695.
- [29] Pasquariello, V., Hickel, S., Adams, N. A., Hammerl, G., Wall, W. A., Daub, D., Willems, S., Gülhan, A., 2015. Coupled simulation of shock-wave/turbulent boundary-layer interaction over a flexible panel. In: *6th European Conference For Aerospace Sciences (EUCASS)*. pp. 1–15.
- [30] Peskin, C. S., 1972. Flow patterns around heart valves: A numerical method. *Journal of Computational Physics* 10 (2), 252–271.
- [31] Piperno, S., Farhat, C., Larroutourou, B., 1995. Partitioned procedures for the transient solution of coupled aeroelastic problems part i: Model problem, theory and two-dimensional application. *Computer Methods in Applied Mechanics and Engineering* 124 (1), 79–112.
- [32] Poinso, T., Lele, S., 1992. Boundary conditions for direct simulations of compressible viscous flows. *Journal of Computational Physics* 101 (1), 104 – 129.
- [33] Qu, Z.-Q., 2010. *Model Order Reduction Techniques: With Applications in Finite Element Analysis*, 1st Edition. Springer Publishing Company, Incorporated.
- [34] Ramm, E., Wall, W. A., 2004. Shell structures - a sensitive interrelation between physics and numerics. *International Journal for Numerical Methods in Engineering* 60 (1), 381–427.
- [35] Rayleigh, J., 1887. *The Theory of Sound*. Dover Publications; 2nd edition.
- [36] Rixen, D., 2001. Generalized mode acceleration methods and modal truncation augmentation. *AIAA paper*, 19th AIAA Applied Aerodynamics Conference, No. 2001–1300.
- [37] Sanches, R., Coda, H., 2014. On fluid-shell coupling using an arbitrary Lagrangian-Eulerian fluid solver coupled to a positional Lagrangian shell solver. *Appl. Math. Model.* 55, 1–18.
- [38] Teixeira, P., Ayruch, A., 2005. Numerical simulation of fluid-structure interaction using the finite element method. *Computers & Fluids* 34 (2), 249–273.

- [39] Toro, E. F., Spruce, M., Speares, W., 1994. Restoration of the contact surface in the HLL-Riemann solver. *Shock Waves* 4 (1), 25–34.
- [40] Vahdati, M., Sayma, A., Imregun, M., 1999. An integrated nonlinear approach for turbomachinery forced response prediction. part i: Formulation. *Journal of Fluids and Structures* 14, 87–101.
- [41] Wilson, E. L., Yuan, M.-W., Dickens, J. M., 1982. Dynamic analysis by direct superposition of Ritz vectors. *Earthquake Engineering & Structural Dynamics* 10 (6), 813–821.
- [42] Wu, L., Tiso, P., 2016. Nonlinear model order reduction for flexible multibody dynamics: a modal derivatives approach. *Multibody System Dynamics* 36 (4), 405–425.